MATERIALS SCIENCE

# In situ recombination junction between p-Si and $TiO_2$ enables high-efficiency monolithic perovskite/Si tandem cells

Heping Shen[1]*, Stefan T. Omelchenko[2]*, Daniel A. Jacobs[1]*, Sisir Yalamanchili[2]*, Yimao Wan[1], Di Yan[1], Pheng Phang[1], The Duong[1], Yiliang Wu[1], Yanting Yin[3], Christian Samundsett[1], Jun Peng[1], Nandi Wu[1], Thomas P. White[1], Gunther G. Andersson[3], Nathan S. Lewis[4†], Kylie R. Catchpole[1†]



**Increasing the power conversion efficiency of silicon (Si) photovoltaics is a key enabler for continued reductions in the cost of solar electricity. Here, we describe a two-terminal perovskite/Si tandem design that increases the Si cell's output in the simplest possible manner: by placing a perovskite cell directly on top of the Si bottom cell. The advantageous omission of a conventional interlayer eliminates both optical losses and processing steps and is enabled by the low contact resistivity attainable between n-type $TiO_2$ and Si, established here using atomic layer deposition. We fabricated proof-of-concept perovskite/Si tandems on both homojunction and passivating contact heterojunction Si cells to demonstrate the broad applicability of the interlayer-free concept. Stabilized efficiencies of 22.9 and 24.1% were obtained for the homojunction and passivating contact heterojunction tandems, respectively, which could be readily improved by reducing optical losses elsewhere in the device. This work highlights the potential of emerging perovskite photovoltaics to enable low-cost, high-efficiency tandem devices through straightforward integration with commercially relevant Si solar cells.**

## INTRODUCTION

The price of silicon (Si) photovoltaic modules has dropped nearly exponentially over the past four decades, with balance of systems costs now accounting for ~70% of a fully installed solar electricity system. Hence further reductions in the cost of Si photovoltaics can be most readily met by increasing the module efficiency and thereby reducing the area-related balance of systems costs. The current laboratory record of power conversion efficiency (η) for single-junction Si solar cells is 26.6%, closely approaching the theoretical limit of 29.4% (*1*). Combining multiple junctions in a single device is one of the most practical and well-demonstrated approaches to exceed this limitation. Efficiencies above the single-junction Shockley-Queisser limit of 32% under 1-sun illumination have been obtained by combining III-V top cells with a Si bottom cell (*2*); however, a number of obstacles impede the commercial viability of this pairing, including the high materials and fabrication costs of III-V semiconductors. Because of their large bandgap tunability, low materials cost, and simple processing requirements, inorganic-organic metal-halide perovskite materials as pioneered by Miyasaka and co-workers (*3*), Park and co-workers (*4*), and Snaith and co-workers (*5*) are attractive candidates for the top cell in a tandem structure with Si. Record efficiencies of 27.3% have been announced for perovskite/Si tandems (*6*), although no details of this cell structure or efficiency have yet been provided in the scientific literature. Compositional engineering of perovskites has also yielded substantial improvements in cell stability (*7*, *8*) while yielding single-junction efficiencies as high as 23.3% (*9*).

Design approaches for creating tandem cells have either two or four electrical terminals per tandem pair. The two-terminal (2-T) configuration allows for monolithic fabrication in which the cells are constructed as a single unit, allowing simple electrical integration at the system level and relaxing the need for additional front and rear transparent electrodes. In place of transparent electrodes, however, the monolithic approach requires an interlayer that effectively facilitates the flow of photogenerated carriers from one subcell to the other. Ideally, this should be achieved with low electrical and optical losses and at minimal processing cost. Tunnel junctions consisting of two heavily doped $p^+$ and $n^+$ regions are a common choice for such an interlayer. The first demonstration of a 2-T perovskite/Si tandem device used a partially crystallized, heavily doped n-type Si layer to form a tunnel junction on top of a crystalline $p^+$-Si emitter in its Si homojunction bottom cell, resulting in η = 13.7% (*10*). Improved light management, combined with advances in perovskite photovoltaics, yielded η = 22.7% by use of heavily doped hydrogenated nanocrystalline Si (nc-Si:H) tunneling layers on a Si heterojunction with an intrinsic thin-layer (HIT) bottom cell (*11*). This approach has been further developed recently by texturing the HIT bottom cell while conformally depositing the perovskite and contact layers using thermal evaporation. Incorporation of an additional nanocrystalline $p^+/n^+$ tunnel junction on top of a heterojunction bottom cell to make a sufficiently conductive recombination junction, along with reduced reflection and an improved infrared response in this design, has yielded an efficiency of 25.2% for a monolithic perovskite/Si tandem solar cell (*12*). Relative to the atomic layer deposition (ALD) $TiO_2$ approach, this method requires an additional [although potentially straightforward in a plasma-enhanced chemical vapor deposition (PECVD) system] processing step and introduces an extra layer that can potentially contribute to parasitic optical absorption. An alternative to using tunnel junctions for interlayer is to use a recombination layer, typically in the form of a transparent conductive oxide (TCO), common choices being indium-doped tin oxide (ITO) (*8*, *13*, *14*) and indium-doped zinc oxide (IZO) (*15*). The previous record efficiency of 23.6% for monolithic perovskite/Si tandems was obtained accordingly by incorporating an ITO intermediate layer to connect a HIT bottom cell and a perovskite top cell (*8*). Impediments to

[1]Centre for Sustainable Energy Systems, Research School of Engineering, The Australian National University, Canberra 2601, Australia. [2]Joint Center for Artificial Photosynthesis, California Institute of Technology, Pasadena, CA 91125, USA. [3]School of Chemical and Physical Sciences, Flinders University, Adelaide, SA 5042, Australia. [4]Division of Chemistry and Chemical Engineering, California Institute of Technology, Pasadena, CA 91125, USA.
*These authors contributed equally to this work.
†Corresponding author. Email: nslewis@caltech.edu (N.S.L.); kylie.catchpole@anu.edu.au (K.R.C.)

further improvements in these TCO-containing interlayer systems include substantial parasitic absorption due to free-carrier absorption at long wavelengths and the prevalence of shunt paths through the top cell, caused by surface roughness (*11*).

We demonstrate herein a third and distinct strategy for fabrication of efficient monolithic, 2-T perovskite/Si tandem solar cells. The approach forgoes the use of a conventional interlayer and instead places the perovskite top cell in direct contact with the Si bottom cell (Fig. 1A). Development of this concept was stimulated by the observation of highly ohmic contact between $TiO_2$ deposited by ALD and p-type Si in photoanodes that efficiently and stably evolve $O_2$(g) from water (*16*). Preliminary testing revealed that despite the absence of an intentional recombination layer between the two materials, a sufficiently conductive contact can be produced to enable the operation of an efficient tandem cell. The contact resistance was subsequently found to be strongly dependent on the band alignment at the $TiO_2$/$p^+$-Si interface and on the relative doping densities of the $TiO_2$ and $p^+$-Si, both of which are sensitive to the $TiO_2$ preparation method. Although in our work $TiO_2$ was prepared by ALD, other studies have shown that under certain deposition and annealing conditions, $TiO_2$ films with similar behavior can be obtained using sputtering (*17*). Hence, analogous behavior may be obtainable with other deposition techniques, including spin coating or spray coating. For our first proof-of-concept tandem devices, we used n-type homojunction Si cells, making their $p^+$ emitter the substrate for a conventional (semitransparent) solution-processed perovskite top cell based on $TiO_2$ and 2,2′,7,7′-tetraakis-(*N*,*N*-di-4-methoxyphenylamino)-9,9′-spirobifluorene (Spiro-OMeTAD). Subsequently, we found that ohmic contact can also be formed between $TiO_2$ and the boron-doped, recrystallized amorphous-silicon (a-Si) layer of a heterojunction cell (*18*), yielding even higher tandem voltages relative to the homojunction. We discuss both cell types herein to demonstrate the general applicability of the interlayer-free concept but primarily make use of the homojunction cells, with their physically simpler structure, to perform our mechanistic analyses.

## RESULTS

The perovskite top cell in our demonstration devices consisted of a conventional n-i-p structure with a stack of cp-$TiO_2$ (compact $TiO_2$)/ms-$TiO_2$ (mesoporous $TiO_2$)/perovskite/Spiro-OMeTAD or PTAA/$MoO_x$/IZO/Au grid, as illustrated in the cross-sectional scanning electron microscope (SEM) image in Fig. 1B. The ALD-deposited $TiO_2$ was uniform and conformal with a low surface roughness of ~0.77 nm (fig. S1A). A ~54-nm thickness of $TiO_2$ was found to be optimal, covered by a ~70- to 80-nm ms-$TiO_2$ layer and an ultrathin PCBM (phenyl-C61-butyric acid methyl ester)/PMMA [poly(methyl methacrylate)] passivation layer to improve the cell voltage and reduce hysteresis in the current-voltage

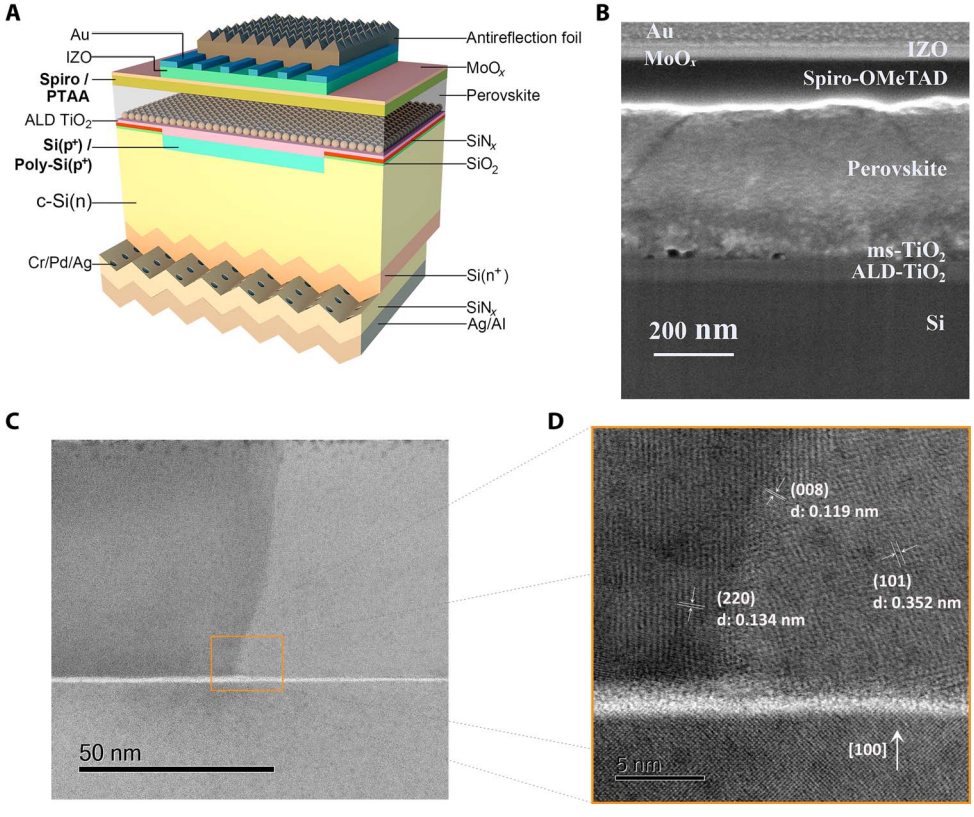


**Fig. 1. Schematic illustration and morphological characterizations of the interlayer-free monolithic perovskite/Si tandem solar cell.** (**A**) Schematic of the interlayer-free monolithic perovskite/crystalline-silicon (c-Si) tandem solar cell (not to scale). Initial tests were carried out on homojunction Si cells with Spiro-OMeTAD (Spiro) as the top perovskite contact; however, our best performance was obtained with polysilicon (poly-Si) bottom cells and PTAA {poly[bis(4-phenyl)(2,4,6-trimethylphenyl)amine]} as the top hole-selective layer. (**B**) Cross-sectional SEM image of the tandem device based on a Si homojunction subcell from the top surface to the $p^+$-Si layer [Spiro-OMeTAD is used as a hole transport material (HTM)]. The antireflection layer was not included because of the large thickness of ~1 mm. (**C**) Scanning transmission electron microscopy (STEM) bright-field (BF) image, and (**D**) high-resolution STEM BF image of the $TiO_2$/$p^+$-Si interface.

(*J-V*) characteristics (*19*). Multication perovskites, which have consistently outperformed their single-cation originators (*7*), were used in the cells and fabricated using an antisolvent one-step method. A composition of $Cs_{0.05}Rb_{0.05}FA_{0.765}MA_{0.135}PbI_{2.55}Br_{0.45}$ yielded stable films with an appropriate bandgap ($E_g$ = 1.63 eV) (*20*). Current matching between the two subcells was obtained by deposition of a relatively thin (~310 nm) perovskite layer. For both 4-T and 2-T Si tandems, a bandgap of ~1.7 to 1.8 eV is expected to yield higher cell voltages (*21*), all other things being equal, than the 1.63-eV bandgap material used herein. At present, the high bandgap perovskites show a greater difference between the bandgap and cell open-circuit voltage ($V_{oc}$) than the more optimized lower bandgap compositions (*7*, *22*, *23*), mitigating the potential gains in voltage. Layer thicknesses of ~120 and ~50 nm (*22*) were used for the organic hole–selective layers (Spiro-OMeTAD and PTAA, respectively). Before sputtering ~40 nm of IZO for the front contact, a 10-nm $MoO_x$ buffer layer was deposited to protect the underlying organic layer from sputter damage.

For the Si bottom cells, we have used both n-type homojunction cells and passivating contact heterojunction cells with pyramidally textured and passivated rear surfaces. Si homojunction cells constitute >80% of the current photovoltaic market share for the moment, primarily on p-type wafers, although a trend toward using n-type substrates as used here is widely anticipated. Passivating contact cells are an emerging technology well suited for tandems, because of their higher cell voltages, simple processing requirements, and strong performance in the infrared (*24*). The heterojunction cell that we used incorporated a thin (<1.4 nm) oxide layer buried beneath ~50 nm of heavily boron-doped, recrystallized a-Si (*18*). For brevity, these devices will be referred to as poly-Si cells, although the top layer is likely a mix of amorphous and partially crystallized silicon.

As a direct demonstration of the interlayer-free concept, Fig. 2A shows the photovoltaic *J-V* performance exhibited by our highest-performing poly-Si tandem cell and the corresponding photovoltaic metrics. The performance of the homojunction tandem is likewise shown in fig. S4D. We obtained a steady-state efficiency of 24.1% for the poly-Si interlayer-free tandem under 100 mW $cm^{-2}$ of simulated air mass 1.5G (AM1.5G) illumination, with a $V_{oc}$ of ~1.76 V, a short-circuit current density ($J_{sc}$) of 17.8 mA $cm^{-2}$, and a fill factor (FF) of ~0.78. Compared to the poly-Si tandems, the best homojunction tandems had a steady-state efficiency of 22.9% (fig. S4D), with slightly lower voltages of ~1.70 V and short-circuit current densities of 17.2 mA $cm^{-2}$. Although both efficiency values are uncertified, the spectral response data predict short-circuit current densities under standard illumination test conditions that are in close agreement with those observed experimentally herein. We thus expect that certified efficiencies would be very similar to the values reported herein. Any spectral mismatch would have its greatest effect on the short-circuit current density, whereas the voltage and FF would be mostly unaffected. These latter metrics are our main concerns for evaluating the interlayer-free concept, as they pertain to the passivation and electrical connection at the subcell interface, respectively.

Stability is a serious issue for all perovskite devices reported in the literature to date. The stability of our devices with respect to heat and moisture was investigated by performing the damp heat test according to the testing protocol 61215 defined by the International Electrochemical Commission (85°C in 85% relative humidity). We performed these tests on encapsulated semitransparent perovskite solar cells with the more thermally stable PTAA as the hole transport layer (HTL; PTAA was also used in the highest-performing perovskite/Si tandem), the perovskite cell being the primary source of instability in our tandems. Data showing the evolution of photovoltaic metrics under aging are provided in fig. S6. These devices maintained ~89% of their original output after testing for >1000 hours, putting them very close to passing protocol 61215, which requires 90% retained efficiency and shows that our cells are well within the stability range established by McGehee and co-workers (*8*) and the more recent work by Ballif and co-workers (*12*). Multiple causes could contribute to the observed performance decreases, including suboptimal encapsulation, degradation of the organic HTM, migration of extrinsic ions introduced into the HTM, and metal electrode diffusion into the perovskite (*25*). Detailed stability results including a discussion of >2500-hour long-term aging data of our homojunction tandems are included in the Supplementary Materials (fig. S9).

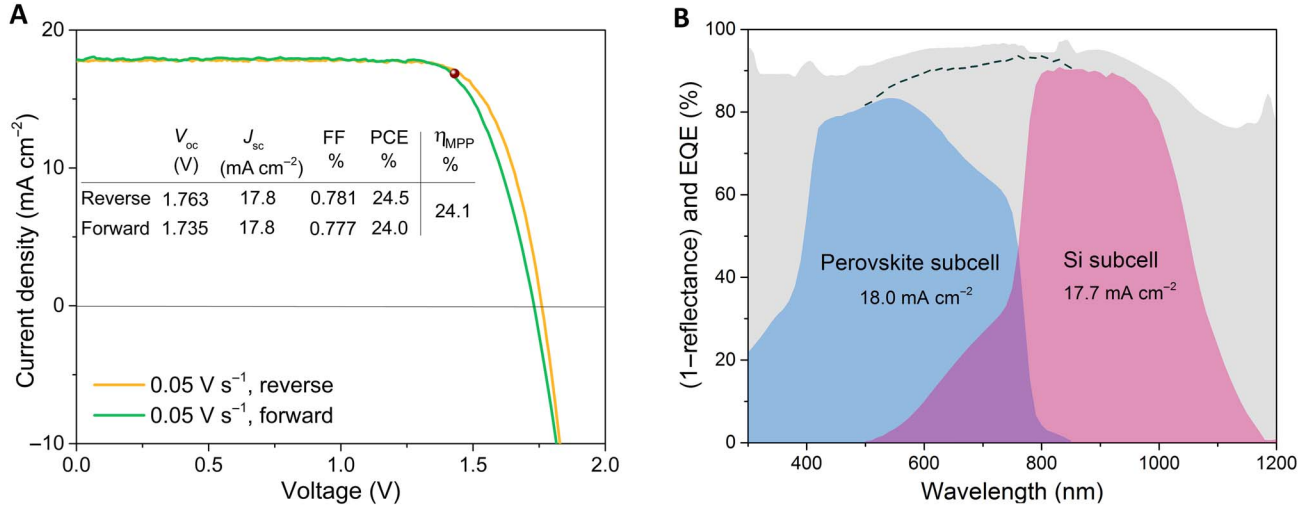


**Fig. 2. Photovoltaic performance and spectral response of the interlayer-free monolithic perovskite/Si tandem solar cell.** (**A**) *J-V* behavior of the proof-of-concept tandem device with both reverse and forward scanning at 0.05 V $s^{-1}$ based on heterojunction poly-Si subcell. (**B**) Absorbance (1–reflectance) of the tandem device (gray shading), external quantum efficiency (EQE) of the perovskite top cell (blue), and EQE of the c-Si bottom subcell (red).

## DISCUSSION

To further investigate the feasibility of the interlayer-free concept, we tested symmetric structures with poly-Si passivation and $TiO_2$ on both sides of the wafer to evaluate the impact of $TiO_2$ deposition on carrier lifetimes. These tests indicated that the poly-Si cell's front-side passivation was not compromised by the ALD-$TiO_2$, as long lifetimes (implied open-circuit voltages of ~701 mV; fig. S5C, green circles) were also observed after deposition. Despite this, the completed poly-Si cells used in our tandems yielded somewhat lower voltages than the implied ~701 mV, pointing to issues with the rear-side passivation, as also indicated by lifetime data (fig. S5C, yellow circles). In our homojunction cells, the $TiO_2$ coating provided partial passivation, yielding implied open-circuit voltages as high as ~650 mV (fig. S5A) under appropriate deposition conditions. Optical losses are a major factor contributing to suboptimal efficiency in our proof-of-concept tandems. Despite adequate current matching, the tandem $J_{sc}$ of 17.8 mA $cm^{-2}$ leaves considerable room for improvement—the deficit of 1.7 mA $cm^{-2}$ compared to the present record $J_{sc}$ of 19.5 mA $cm^{-2}$ (*12*) is worth as much as 2.1% in absolute efficiency. These optical losses stem from substantial reflections at the perovskite front side and the Si interface, in addition to front-side parasitic absorption in the organic hole–selective layer (*13*). The current record-holding device has shown that both reflection sources can nearly be fully eliminated by fabricating a device on a Si cell with front-side random pyramids (*12*). Our primary innovation of an interlayer-free tandem cell appears fundamentally compatible with front-textured Si cells, because conformal ALD-$TiO_2$ can be easily deposited on these structures. Our proof-of-concept design, with its reliance on a solution-processed perovskite cell, is not readily compatible with large-scale texturing. Nonetheless, textures with a smaller feature size ("nanotexturing") may be compatible with solution-processing a conformal perovskite layer and may confer similar advantages in terms of antireflection (*26*). Better light management can also be envisaged via tuning of the perovskite composition and reduction of the optical absorption and reflection from the front-side selective contact (*27*).

Efficient operation of the interlayer-free tandem device requires facile charge transfer between the Si cell's front surface and the $TiO_2$ layer. Specifically, photogenerated electrons collected in the $TiO_2$ layer must be able to recombine, while incurring minimal voltage loss, with corresponding holes from the Si emitter region. The n-type character of $TiO_2$ would be expected to produce a rectifying p-n heterojunction with p-type Si, whether monocrystalline, polycrystalline, or amorphous (*28*). Despite this, the *J-V* characteristics of our tandem devices did not exhibit S-shaped curves, nor the FF losses that would be expected if a rectifying contact were present (*29*). To explicitly demonstrate the existence of facile electrical contact between $TiO_2$ and p-type Si, we used the structure depicted in Fig. 3A to investigate the electrical properties of the $TiO_2$/$p^+$-Si interface in our homojunction tandem devices—the operating principles for our poly-Si tandems presumably being similar. Analogous test structures were also fabricated using an ITO film instead of $TiO_2$ to emulate the recombination layer used in previous tandem designs (*8*, *13*, *14*). The contact resistivity ($\rho_c$) of a given film with respect to $p^+$-Si was determined via the method devised by Cox and Strack (*30*). We note that values derived include not only the desired metal oxide/$p^+$-Si contact resistivity but also the bulk metal oxide as well as the oxide/Al contact resistance, so these measurements are to be interpreted as an upper bound on the former quantity. In our initial tests of the $TiO_2$/$p^+$-Si interface, all samples exhibited a relatively high contact resistance as seen in Fig. 3B, which was only improved upon annealing at 400°C in dry air. After annealing, the highest-performing $TiO_2$ samples achieved a contact resistance better than 30 milliohm·$cm^2$, surpassing that of the ITO samples at ~230 milliohm·$cm^2$ by a wide margin. By contrast, annealing had a detrimental effect on the ITO/$p^+$-Si contact, correlating with a previous observation of reduced bulk conductivity when annealing ITO on quartz (*13*). Subsequent testing has revealed that while helpful, the annealing step is not necessary for the $TiO_2$/$p^+$-Si contact because acceptably low resistivity (~100 milliohm·$cm^2$) was achieved without annealing, by instead increasing the ALD chamber temperature from 75° to 200°C (fig. S13A). Regarding the comparison with ITO, tandem devices fabricated with ITO as a recombination layer exhibited overall inferior photovoltaic performance as determined by all device metrics, with $V_{oc}$ = 1.510 V, $J_{sc}$ = 15.8 mA/$cm^2$, and FF = 0.637 (fig. S10D). The current loss in this test device is likely a result of parasitic absorption in the ITO layer and reflection loss on the ITO/Si interface, and the reduced $V_{oc}$ and FF are ascribable to inferior contact between the subcells (as supported by the *J-V* measurements of Fig. 3B), as well as shunting due to pinholes in sputtered ITO layers. This indicates that our interlayer-free tandem cells can not only be fabricated in fewer steps but also enjoy performance benefits relative to the standard design incorporating an ITO-based recombination layer.

It is notable that $TiO_2$ layers prepared using different ALD precursors yielded markedly mutually different *J-V* characteristics in our $TiO_2$/$p^+$-Si test structures, as highlighted in Fig. 3B. Ohmic, highly conductive behavior between $TiO_2$ and $p^+$-Si was observed in samples with $TiO_2$ prepared using tetrakisdimethylamidotitanium (TDMAT) as the ALD precursor (Fig. 3B, green solid line), whereas by contrast, very low conductivity ($\rho > 10$ ohm·$cm^2$) in the low-bias region was obtained when using titanium tetrachloride ($TiCl_4$) instead (Fig. 3B, blue solid line), despite otherwise identical processing conditions. The use of titanium tetraisopropoxide (TTIP) resulted in intermediate performance, displaying conductive but distinctly nonlinear *J-V* behavior (Fig. 3B, yellow solid line). The conductivity of these $TiO_2$/$p^+$-Si test structures was found to correlate well with the behavior of tandem devices constructed using the same material, with $\eta$ = 21% obtained for homojunction tandems using TTIP as the precursor (fig. S10E) and $\eta$ = 3.6% for $TiCl_4$ as the precursor (75°C deposition; fig. S10F). These marked variations motivated the need for a fundamental understanding of the contact between $TiO_2$ and $p^+$-Si. Below, we present arguments that indicate that the contact is mediated by interfacial defects, a distinct mechanism to the one that predominates in conventional p-n tunnel junctions.

One aspect of clear relevance to the transport of carriers between $TiO_2$ and Si is the interfacial band alignment, whatever the underlying mechanism. On the basis of x-ray photoelectron spectroscopy (XPS) measurements of the electron affinity ($\chi^{TiO_2}$) for our $TiO_2$ samples (4.35 to 4.7 eV; fig. S12) and the Si ionization energy (I.E.$^{Si}$), taken here as 5.15 eV, the band alignment at an idealized $TiO_2$/$p^+$-Si junction should result in an energy gap of $\Delta = E_c^{TiO_2} - E_v^{Si} = \chi^{TiO_2} - \text{I.E.}^{Si} \approx$ 0.45 to 0.8 eV, between the top of the Si valence band and the bottom of the $TiO_2$ conduction band (Fig. 3C). Less idealized, experimental determinations of $\Delta$ that include the surface dipole contribution require combining data from several techniques and have only been reported rarely for $TiO_2$/p-Si interfaces (*31*). In those studies, values of $\Delta$ between 0.45 and 0.8 eV were obtained depending strongly on the 1- to 2-nm interlayer composition, which could partly account for our observation of a pronounced sensitivity to processing. A nonvanishing gap at the

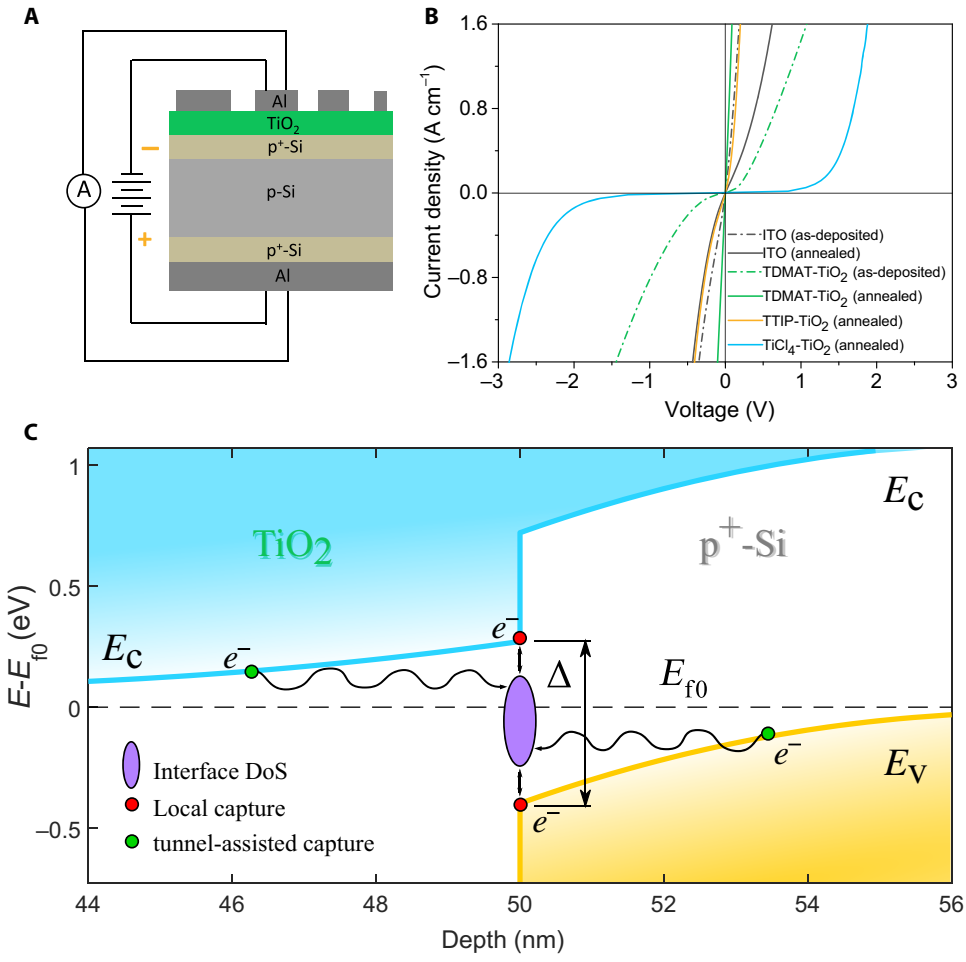


**Fig. 3. Contact behavior and simulated band diagram of $TiO_2$/$p^+$-Si interfaces.** (**A**) Schematic of the structure used for measuring contact resistivity. (**B**) Comparison of the *J-V* behavior of ITO/$p^+$-Si and various $TiO_2$/$p^+$-Si structures before and after annealing at 400°C in air. $TiCl_4$-ALD $TiO_2$ listed here is deposited with a reactor chamber temperature of 75°C. (**C**) Simulated band diagram of the $TiO_2$/$p^+$-Si at equilibrium assuming n-type doping of $5 \times 10^{18}$ $cm^{-3}$ on $TiO_2$ and $10^{19}$ $cm^{-3}$ for $p^+$-Si (appropriate for our test structure with TDMAT $TiO_2$; see table S3). The unknown interfacial energy gap Δ is shown here for illustrative purposes as 600 meV, which falls within the range of reported measurements (*31*). Both mechanisms of direct- and tunneling-assisted capture by interfacial density of states (DoS) are shown.

$TiO_2$/$p^+$-Si interface prohibits band-to-band tunneling between the $TiO_2$ conduction band and the Si valence band at 0 V as would occur in a standard tunnel junction, because of a lack of overlap in the bulk density of states at equilibrium (see Fig. 3C). Under sufficient reverse bias, the necessary overlap will occur, but carriers would then need to tunnel through the sum of the depletion and interlayer widths, estimated to be tens of nanometers for $TiO_2$ doping in the range of $10^{17}$ to $10^{19}$ $cm^{-3}$. This distance is at the upper limit of what is physically reasonable and indicates that band-to-band tunneling at reverse bias is only likely to occur when both depletion regions are very small, corresponding to high doping (*32*). At forward bias, the band overlap is decreased, and band-to-band tunneling becomes prohibited, requiring a separate mechanism to explain the presence of a high forward current. In place of tunneling, at forward bias, a current could be carried via the thermionic emission of conduction-band electrons from $TiO_2$ over the barrier due to the conduction band offset $E_g^{Si} - \Delta$, but this would predict a strong trade-off between the forward and reverse current, contrary to the observed ohmic behavior (i.e., large gaps Δ would provide a small barrier for the forward thermionic emission current while enlarging the threshold voltage for reverse tunneling current and vice versa). We conclude that our observation of high conductivity in both the forward and reverse directions is indicative of an operating mechanism distinct from that of a familiar p-n tunnel junction.

The considerations above indicate that the presence of a pristine interfacial energy gap Δ is not readily compatible with the observed highly conductive contact between $TiO_2$ and $p^+$-Si. A more likely alternative is the presence of a substantial density of localized midgap states at the interface between Si and $TiO_2$. These interfacial states can facilitate band-to-band tunneling at reverse bias and act as generation-recombination centers at all bias voltages (*29*, *33*). In such a scenario, electrons move into and out of the defect states via local capture/emission as well as tunneling (Fig. 3C). As generation-recombination centers, the interface states would have a substantial influence on charge transport by facilitating the recombination of majority carriers in Si at forward bias without requiring emission over the interfacial barrier. At reverse bias, every recombination center becomes a source of generation, and high conductivity can be obtained by thermally generated carriers. Conceptually, this situation is similar to having a recombination layer of atomic dimensions between $TiO_2$ and $p^+$-Si, created in situ and intrinsically via the native material contact, without the introduction

of substantial optical losses. For the contact resistance, the relevant recombination induced by the interfacial defects occurs between majority holes in the p-Si and electrons in $TiO_2$, just as in a conventional (e.g., ITO) recombination layer. These defects may also induce unwanted recombination between majority holes and minority electrons in $p^+$-Si, thereby degrading the open-circuit voltage of the bottom cell. In homojunction cells, minority carriers are capable of reaching the $TiO_2$ interface, making this a relevant concern. In contrast, in passivating contact cells, these defects will not affect the degree of passivation because of the selective barrier (buried oxide in the poly-Si design) between minority carriers and the $TiO_2$ interface. Hence, in homojunction cells, the interfacial defects must be carefully controlled so as not to overly compromise the silicon cells' voltage, whereas in selective-contact designs, this trade-off should be largely alleviated, depending on the degree of selectivity.

We used numerical drift-diffusion models based on the Solar Cell Capacitance Simulator to investigate the impact of interfacial generation-recombination centers on the interfacial contact resistance. These models were designed to compute the current across a $TiO_2/p^+$-Si heterojunction, assuming ohmic metal contacts on both sides, and therefore mainly addressed the junction current, with only minor contributions from bulk conduction through the small layer thicknesses (50 and 100 nm for $TiO_2$ and Si, respectively). Shockley-Read-Hall (SRH) recombination centers were added at the $TiO_2/p^+$-Si interface to physically correspond to localized states that are expected to form in the interfacial energy gap. These defects are likely to occur at a high density, given the relatively low degree of lattice matching between $TiO_2$ and Si, the possibility of precursor remnants, Si dangling bonds, and the presence of a 1- to 2-nm amorphous alloy interlayer observed in our samples between the two bulk crystals (Fig. 1, C and D). Interlayers are known to have a profound effect on the interface dipole or band alignment of semiconductor-semiconductor contacts, as well as on the mechanisms of charge transfer (*34*), and may therefore play a key role in our experimental system. For simplicity in our modeling, the contribution of the interlayer capacitance was neglected, while the defect density of the interlayer was captured in the interfacial SRH parameters. Tunneling due to defects was not accurately modeled because of a lack of detailed knowledge of the interface parameters, but calculations with tunneling processes included are presented in Fig. 4A and fig. S15 to qualitatively illustrate the behavior that results from this effect.

Figure 4A shows the computed *J-V* characteristics of a $TiO_2/p^+$-Si heterojunction with varying gaps $\Delta$ in the range of 0.4 to 0.9 eV and with a high density of neutral midgap defects (surface recombination velocities $S_n = S_p = 10^5$ cm $s^{-1}$), all other parameters being equal (see table S3). These *J-V* characteristics bear a notable resemblance to the experimental behavior of Fig. 3B, in that they both exhibit the full range of qualitative characteristics seen experimentally, namely, highly conductive ohmic behavior (e.g., $\Delta = 0.4$), asymmetric exponential-type curves ($\Delta = 0.5$ and 0.6 eV), and strong rectification ($\Delta = 0.7$ to 0.9 eV). The detrimental effect of a large band offset can only be compensated by higher recombination velocities up to the physical limit of $S_{n,p} = v_{th} \approx 10^7$ cm $s^{-1}$, likely ruling out high defect-mediated conductivity for band offsets greater than ~0.7 eV. A somewhat less trivial prediction of the SRH model concerns the balance of carrier densities at the interface. According to eq. S1, the interfacial carrier densities must be balanced to achieve maximal conductivity (particularly, $v_n n_0 \approx v_p p_0$ where $n_0$ and $p_0$ are the equilibrium carrier densities at the interface and $v_{n,p}$ their quasi-recombination velocities). Experimentally, the interfacial conductivity was found to benefit from a high substrate doping (Fig. 4B, red markers), which is consistent with donor-type defects at the interface that require excess acceptors to achieve the relevant balance. Donor defects are frequently present at both $TiO_2$ and unpassivated Si surfaces in the form of oxygen vacancies and dangling bonds ($P_b$ centers) (*35*), respectively. The SRH theory thus consistently accounts for the ohmic conductivity between $TiO_2/p^+$-Si, in accord with the behavior observed previously for $TiO_2$-protected Si photoanodes (*16*).

According to the SRH theory outlined above, the diverse behavior seen in Fig. 3B with respect to preparation conditions likely results from variations in the band offset between the $TiO_2$ conduction band edge and the Si valence band ($\Delta$), as well as in the $TiO_2$ doping density and interfacial defect properties. In accordance with this picture, our highest-performing material in the homojunction designs was TDMAT-ALD $TiO_2$, which exhibited relatively large electron affinities for anatase (fig. S12A). Although vacuum levels are only an approximate indicator of the actual band alignment, the data suggest a small $\Delta$, in addition to a sufficiently conductive $TiO_2$ layer (table S3), is helpful for obtaining a high-conductivity contact to $p^+$-Si. This raises a related issue regarding the $TiO_2$ work function's influence on the perovskite cell's built-in or flat-band voltage. A larger n-type selective contact work function predicts a reduced built-in voltage, all other things being equal, and therefore a reduced perovskite $V_{oc}$. This is contrary to our experimental observation that the perovskite cells on TDMAT-ALD $TiO_2$ function without substantial losses to their open-circuit voltage. The observed cell performance is thus indicative that the ms-$TiO_2$ layer inserted between the cp-$TiO_2$ layer and the perovskite in the standard cell architecture functions to maintain the top-cell voltage, likely due to its smaller work function (*19*). Single-junction perovskite cells fabricated without a ms-$TiO_2$ layer (i.e., directly on the TDMAT-ALD $TiO_2$ compact layer) markedly exhibited reduced open-circuit voltages as predicted by the preceding argument (fig. S14A; note that this does not indicate an intrinsic limit of planar cells, as solution-processed compact layers yielded uncompromised, high open-circuit voltages). This reasoning is also supported by our drift-diffusion simulations of single-junction perovskite solar cells with and without a mesoporous layer (fig. S14B). The mechanism of work function adjustment imputed to the ms-$TiO_2$ is illustrated in the simulated band diagram of Fig. 4C. Devices whose compact titania layers have a large work function (e.g., our TDMAT-ALD $TiO_2$) therefore seem to benefit substantially from inclusion of the mesoporous layer. Mesoporous layers are typically annealed at high (~400°C) temperatures to drive off the organic suspension agents, but options exist for low-temperature preparation (*36*) and for the deposition of layers with analogous functionality that do not require heat treatment (*37*). As a preliminary demonstration of a low-temperature interlayer-free process, we fabricated tandems with open-circuit voltages as high as ~1.75 V (fig. S14C) without exceeding 200°C in the processing sequence, by optimizing the $TiCl_4$-ALD $TiO_2$ (fig. S13A). With its lower work function (fig. S13D), $TiCl_4$-ALD $TiO_2$ allows uncompromised top-cell voltages in a planar architecture without ms-$TiO_2$, although wetting issues in the perovskite deposition seem to have compromised the FFs of these cells. This behavior is a common issue for solution-processed planar cells but can be addressed by low-temperature interface engineering (*38*).

According to our analysis, an enabling feature of interlayer-free tandems is the presence of intragap states that bridge the energetic offset between the Si subcell and the adjoining contact layer ($TiO_2$ in our demonstration). For homojunction Si cells, minority carriers may recombine at the same defects, compromising the Si cell's voltage.

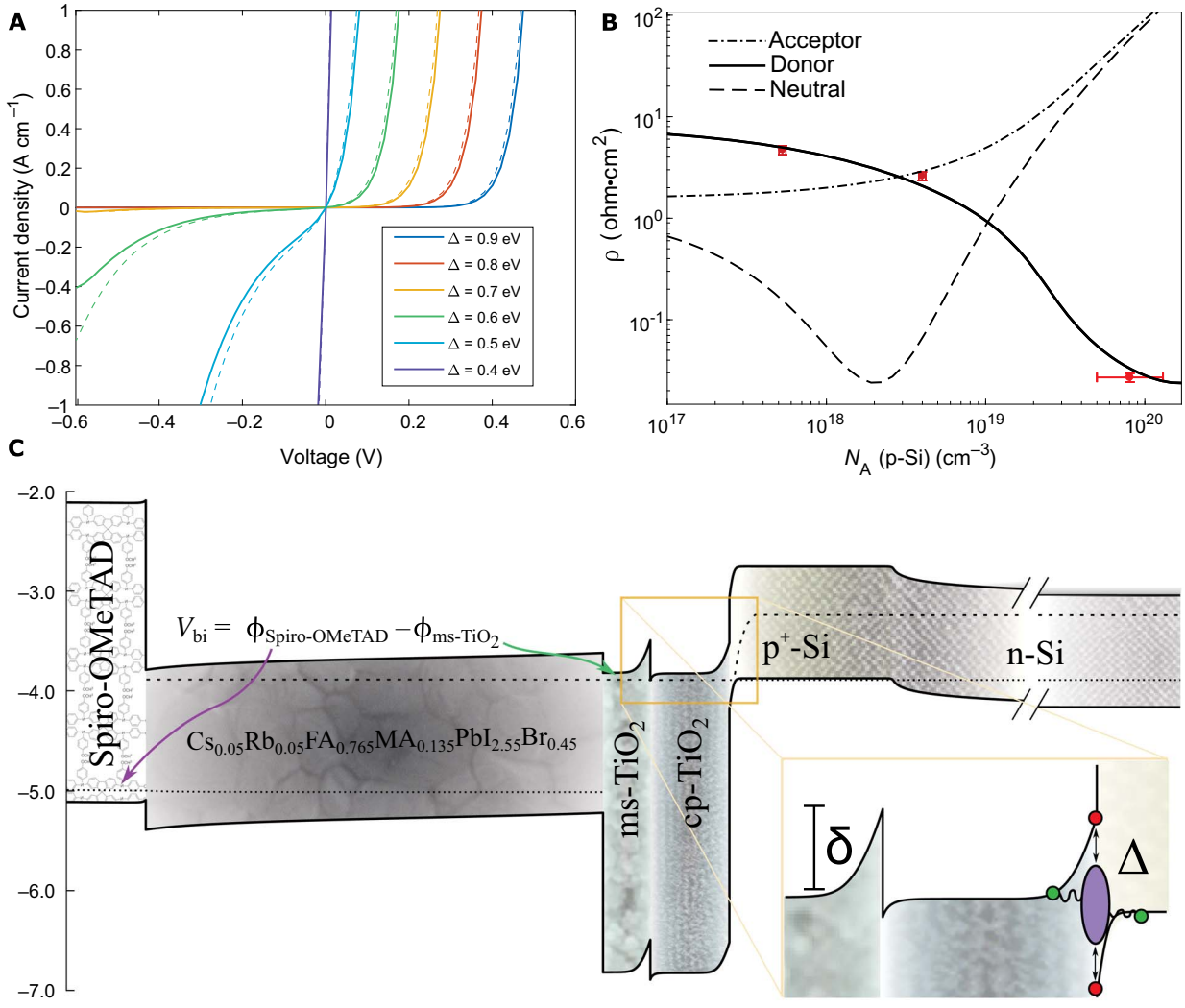


**Fig. 4. Mechanism understanding of low contact resistivity of $TiO_2$/p$^+$-Si interfaces and simulated band diagram of the full tandem device.** (**A**) Simulated *J-V* behavior for varying interfacial gaps Δ. A single neutral midgap SRH defect was included with $S_n = S_p = 10^5$ cm s$^{-1}$. The dashed curves are computed with tunneling to defects included. (**B**) Simulated small voltage resistivity $\left(\rho = \frac{dV}{dJ}|V = 0\right)$ with the $TiO_2$ donor density fixed at $10^{18}$ cm$^{-3}$ and variable p-Si acceptor doping, $N_A$. Measurements are included as data points in red. Calculations for neutral (dashed line), acceptor type (dotted-dashed line), and donor type (solid lines) are shown to demonstrate the important effect of defect charge on the interfacial carrier balance. (**C**) Simulated band diagram of the full tandem device based on a homojunction Si subcell with high work-function cp-$TiO_2$ at illuminated open circuit. The inset depicts the two important energetic offsets Δ and δ, respectively, defined as the valence-to-conduction band offset at the $TiO_2$-Si interface and the difference in work functions between our solution-processed ms-$TiO_2$ layer and that of the ALD compact layer.

Nonetheless, for the homojunction cells with $TiO_2$, we obtained open-circuit voltages of 654 mV (fig. S5A) in just a few attempts while retaining an adequate contact resistance of 0.96 ohm·cm$^2$ (fig. S5B), suggesting that considerable room for improvement using homojunctions may remain in achieving the optimal balance between passivation and contact resistance. For perovskite/Si tandems, the issue of series resistance is much less severe [by a factor of ~5 (*39*)], because of the higher voltage and lower cell current. For the poly-Si cell, this trade-off is entirely avoided because of the carrier-selective buried oxide layer, which blocks the passage of minority carriers to the $TiO_2$ interface (*18*). Carrier selectivity, a common feature among passivating contact designs, allows the $TiO_2$ interfacial defect density to be freely tuned for optimal contact resistance without detrimentally affecting the $V_{oc}$ of the Si cell. Considering the already superior performance of passivating contact–type cells for use in tandems, the interlayer-free concept seems most promising for these cells as compared with homojunction designs.

In conclusion, we have demonstrated two proof-of-concept 2-T perovskite/Si tandem devices that function without a conventional interlayer between their subcells. In principle, this concept may be generalized to other cell designs including those based on the use of HIT silicon, as well as newer passivating contact Si cells (*24*). Whereas fabrication of an nc-Si tunnel junction interconnect is relatively straightforward for HIT cells, these layers introduce a small but potentially important amount of parasitic loss in the region of ~550 to 700 nm (*16*), where the nc-Si is absorbing and the perovskite top cell's absorption is simultaneously incomplete. Optical calculations indicate that this loss can be as large as ~1.0 to 1.5 mA cm$^{-2}$ under the AM1.5G spectrum for standard tunnel junction thicknesses. Larger losses can be expected for ITO recombination layers deposited without annealing

(*16*). The interlayer-free concept thus offers dual advantages of simpler processing and reduced optical losses compared to TCO and tunnel junction interlayers. We identified suboptimal optics on our tandem device's front side as the main performance limitation in our demonstration devices, which could be markedly improved using a silicon cell with front-surface texturing for antireflection and thinner, less absorbing HTMs. The contact between $TiO_2$ and Si should not be substantially affected by micron-scale texturing, making the interlayer-free design described here fully compatible with evaporating a perovskite top cell onto a textured Si wafer, which leads to very low optical losses (*12*). In principle, the desired device properties can also be obtained from a variety of $TiO_2$ deposition and processing conditions and from other materials. The publication of a similar scheme using $SnO_2$ (*40*) instead of $TiO_2$ while this paper was under review demonstrates the wide applicability of the interlayer-free concept. Jointly, our work highlights the potential of emerging perovskite photovoltaics to enable low-cost, high-efficiency tandem devices through straightforward integration with commercially relevant and emerging Si solar cells.

## MATERIALS AND METHODS

### Chemicals

All chemicals were used as received without further purification. Mesoporous transparent titania paste (30 NR-D), methylammonium iodide, formamidinium iodide (FAI), formamidinium bromide, and methylammonium bromide (MABr) were purchased from Greatcell Solar. $MoO_x$ powder was procured from Alfa Aesar, and all other materials [including cesium iodide (CsI) and rubidium iodide (RbI)] were obtained from Sigma-Aldrich. TTIP, $TiCl_4$, and TDMAT were used as the ALD precursors for making cp-$TiO_2$ films.

### Fabrication of c-Si solar cell

A 200-μm-thick n-type float zone Si wafer with a resistivity of ~1 ohm·cm was used as the substrate. Both sides of the wafers were chemically polished and coated with a thick $SiO_2$ layer (~100 nm) via a 1050°C dry oxidation process. The wafers were then immersed in 1% (volume %) hydrofluoric acid (HF) to remove the $SiO_x$ on the back side while the front side was protected with a coating of photoresist (AZ 1518). A texturing process was then performed on the back side on which $SiO_2$ was subsequently grown using a wet oxidation process. The oxide on the front side was then removed from the active region for boron doping of the $p^+$ emitter using photolithography, which defined the cell area of 1 cm by 1 cm. Boron diffusion was performed by transferring the wafers into a Tempress quartz tube furnace at 930°C with deposition for 25 min and oxidation for 20 min. Next, phosphorus diffusion doping ($POCl_3$) was performed on the rear side with wafers back to back, at a diffusion temperature of 780°C for 30 min. The borosilicate glass on the front side and the phosphosilicate glass on the rear side were then removed using an HF etch. The front side was then covered with ~10-nm $SiO_2$ from dry oxidation process, followed by PECVD $SiN_x$ (refractive index of ~1.9, ~90 nm thick). The textured rear side was then passivated with $SiN_x$ (refractive index of ~1.9, 70 nm thick) deposited by PECVD at 500°C. The back side used a point-contact scheme. Photolithography was used to remove the $SiO_2/SiN_x$ stack on the front active area and define the contact opening for the rear side of the wafter. A buffered HF etch was then used to remove the passivation layers in the contact regions. A Cr (18 nm)/Pd (18 nm)/Ag (25 nm) metal stack was thermally evaporated on the rear side of the wafer, followed by liftoff of excess metal with acetone in an ultrasonic bath. The Cr/Pd/Ag rear-contact stack, remaining in dots, was then covered with a Ag (100 nm)/Al (500 nm) contact capping layer using thermal evaporation.

For the poly-Si solar cell, the rear-side design was the same as the homojunction Si solar cell, while the front side had a thin (<1.4 nm) oxide layer buried beneath ~50 nm of heavily boron-doped, recrystallized a-Si. The fabrication process of the front $SiO_x$/poly-Si stack was the same as in (*18*), where a-Si was deposited by PECVD and further doped with boron at 850°C for 30 min.

### Preparation of ALD-$TiO_2$ layer

A cp-$TiO_2$ layer, derived from one of three different precursors, TDMAT, TTIP, and $TiCl_4$, was deposited directly on top of $p^+$-Si after removal of the Si native oxide with an HF etch. Immediately after the HF etch, the Si solar cells were transferred to the ALD chamber for $TiO_2$ deposition.

For deposition using the TDMAT precursor, an Ultratech Fiji 200 Plasma ALD system was used, with the reaction temperature fixed at 150°C. The TDMAT precursor was maintained at 75°C. Before ALD, a 0.10-s pulse of $H_2O$ was applied to the sample. Each ALD cycle consisted of a 0.015-s pulse of $H_2O$, followed by a 0.10-s pulse of TDMAT. Between each precursor pulse, a 15-s purge under a constant flow (0.02 liters $min^{-1}$) of research-grade $N_2$(g) was used. While idle, the ALD system was maintained under a continuous $N_2$(g) purge and at a pressure of ~0.5 torr.

A thermal ALD system (TFS200, BENEQ) was used for depositing $TiO_2$ films using the TTIP or $TiCl_4$ precursors, with $N_2$(g) as the purge gas. For the $TiCl_4$ precursor, in our initial tests, the reactor temperature was set to be 75°C, and $H_2O$ was used as the oxidant. The chamber $N_2$(g) flow was set to be 200 standard cubic centimeters per minute (sccm). Each ALD cycle consisted of a 0.75-s pulse of $TiCl_4$ followed by a 0.050-s pulse of $H_2O$. Between each precursor pulse, a 0.75-s purge under a constant flow (300 sccm) of research-grade $N_2$(g) was used. The deposition rate was ~0.76 Å $cycle^{-1}$ measured by spectroscopic ellipsometry (M2000, J.A. Woolam). We further varied the $TiCl_4$-ALD fabrication processes by raising the reactor temperature to 150° and 200°C, with all other conditions unchanged. These films were then incorporated into testing structures for contact and passivation measurements and were used in the low temperature–processed 2-T perovskite/Si tandem.

For the TTIP precursor, the source was heated to a temperature of 40°C, and the reactor was set to a temperature of 230°C. $H_2O$ was also used as the oxidant. Each ALD cycle consisted of a 1-s pulse of TTIP, followed by a 0.5-s pulse of $H_2O$. Between each precursor pulse, a 2-s purge under a constant flow (300 sccm) of research-grade $N_2$(g) was used. The deposition rate was determined to be ~0.023 Å $cycle^{-1}$.

### Standard ITO recombination layer deposition

To compare the behavior of ALD-$TiO_2$ with the widely used ITO recombination layer, ITO was sputtered on the $p^+$-Si substrates using an ATC 2400-V sputtering system from AJA International Inc. Samples were sputtered using a radio frequency (RF) source maintained at 30 W under an Ar plasma. The chamber pressure was maintained at 1.5 mtorr during deposition. By depositing for 1 hour, the resultant ITO thickness was ~40 nm.

### Preparation of the perovskite solar cell

#### *Electron transport material and passivation layer deposition*

To complete the tandem device, a ~70- to 80-nm ms-$TiO_2$ layer was deposited on either the ALD-$TiO_2$ layer or the ITO recombination layer

by spin-coating diluted $TiO_2$ paste ($TiO_2$/ethanol, 1:12, w/w) at a speed of 5000 rpm. The as-prepared film received a high-temperature treatment at 400°C for 20 min, which was performed in air. Immediately, after cooling to room temperature, the substrate was further passivated with an ultrathin layer by spin-coating a PMMA/PCBM mixture (1:3, w/w) in chlorobenzene at 5000 rpm $s^{-1}$ with a ramp of 5000 rpm $s^{-1}$ for 30 s (*20*). The sample was subsequently baked on a hotplate at 100°C for 10 min.

***Perovskite deposition***

The multiple-cation perovskite precursor solution ($Cs_{0.05}Rb_{0.05}FA_{0.765}MA_{0.135}PbI_{2.55}Br_{0.45}$) contained 1.2 M $PbI_2$, 1.1 M FAI, 0.20 M $PbBr_2$, 0.20 M MABr, 0.091 M CsI, and 0.039 M RbI in 1 ml of anhydrous *N*, *N*′-dimethylformamide (DMF)/dimethyl sulfoxide (DMSO) (8:2, v/v). Different spin-coating speeds and precursor solution concentrations were used to tune the perovskite film thickness.

In Approach 1 using the two-step perovskite fabrication process, the multiple-cation perovskite precursor solution was deposited by spin coating at 2000 rpm with a ramp rate of 200 rpm $s^{-1}$ for 10 s and then at 4000 rpm with a ramp of 1000 rpm $s^{-1}$ for 25 s. During the second step, ~100 μl of chlorobenzene was poured on the spinning substrates 5 s before the end of the program.

In Approach 2, modified perovskite fabrication process was used to make the perovskite top cells in the tandem device to reduce the perovskite thickness and ensure current matching. One ml of the multiple-cation perovskite precursor solution in Approach 1 was diluted with 0.2 ml of anhydrous DMF/DMSO (8:2, v/v) to obtain a 1.0 M concentration of $PbI_2$. In addition, the chlorobenzene dropping was conducted ~8 s before the end of the second spinning stage, while all other parameters were kept the same with those in Approach 1.

In Approach 3, to further reduce the perovskite film thickness for the tandem device, the second stage of the spin-coating process was modified additionally by increasing the ramp speed from 1000 to 4000 rpm $s^{-1}$ and changing the chlorobenzene dropping to ~10 s before the end of the program.

In all cases, the spin-coated perovskite films were immediately annealed for 30 min at 100°C after the spin-coating process was completed. We note that the perovskite film fabricated here is also compatible with the modified two-step vacuum flash method for high reproducibility (*13*). To assess the perovskite quality, single-junction perovskite devices were fabricated on clean fluorine doped tin oxide (FTO) substrates using a standard process that has been optimized for making state-of-the-art devices (*19*, *20*). The optimized process for perovskite film deposition was straightforwardly used for fabricating the perovskite/Si tandem device.

***HTM and contact deposition***

A Spiro-OMeTAD precursor solution was prepared by dissolving 72.5 mg of Spiro-OMeTAD, 28.5 μl of 4-tert-butylpyridine (TBP), and 17.5 μl of lithium bis(trifluoromethanesulfonyl)imide (LiTFSI) solution (520 mg $ml^{-1}$ in acetonitrile) in 1 ml of chlorobenzene. The Spiro-OMeTAD thin film was deposited by spin-coating the precursor solution at 3500 rpm with a ramp of 3500 rpm $s^{-1}$ for 30 s. After spin-coating the Spiro-OMeTAD solution, the substrates were placed in a humidity-controlled box for 12 hours to allow the oxidation of the Spiro-OMeTAD film before electrode/contact layer deposition. The PTAA HTM was fabricated by spin-coating a PTAA solution at 3000 rpm for 30 s with an acceleration rate of 3000 rpm $s^{-1}$. The PTAA solution consisted of PTAA (10 mg $ml^{-1}$) with an additive of 7.5 μl of LiTFSI in acetonitrile (170 mg $ml^{-1}$) and 4 μl of 4-TBP in 1 ml of toluene. Approximately 10 nanometers of $MoO_x$ was deposited on the samples by thermal evaporation at a rate of 0.05 nm $s^{-1}$ under a high vacuum of $8 \times 10^{-7}$ torr. The front transparent contact was then fabricated by sputtering ~40-nm IZO on the $MoO_x$. The sputtering was performed for 60 min with 30 W of RF power under an Ar plasma, with a chamber pressure of 1.5 mtorr. To complete the device, Au fingers with a period of 1 mm and a width of 30 μm (3% shading) were deposited on the sample using e-beam evaporation through a shadow mask. A homemade textured foil was applied on the front surface of the complete tandem device (*13*).

The single-junction perovskite solar cells in this work use the same composition and deposition process as those used in the tandem device. The semitransparent device had the same front contact configuration as that in the tandem device, while the opaque perovskite solar cells have the full cell area deposited with gold on top of HTM. For encapsulation, the solar cells were placed between two pieces of glass, and edge sealing was performed using butyl rubber. No ethylene vinyl acetate for lamination was applied in our encapsulation.

## Contact resistivity measurement

The electrical contact behavior of the $p^+$-Si/ALD-$TiO_2$ structure was evaluated by $\rho_c$ measured using the method devised by Cox and Strack (*30*). The $p^+$-Si/ALD-$TiO_2$ contacts were fabricated on planar p-type c-Si wafers with a resistivity of approximately 1 ohm·cm and a thickness of 250 μm. Both sides of the c-Si wafer were doped with boron using the same recipe used in solar cell fabrication. The doped wafers were then RCA (Radio Corporation of America)–cleaned and then subjected to a dilute HF etch. One side of the doped wafer was then coated with an ALD $TiO_2$ or ITO layer. An array of circular pads with different diameters of Al was evaporated on this side via a shadow mask. The pad sizes were 0.1066, 0.1465, 0.1955, 0.2400, 0.3025, 0.4098, 0.5960, 0.7905, or 0.9828 $cm^2$. These sizes are determined by the hole sizes made on the shadow mask, which was prepared by laser cutting. The back side of the wafer was capped with a full area Al film. Current-voltage (*I*-*V*) measurements were performed at room temperature using a Keithley 2425 source meter. The resistance versus diameter trend was fitted with a spreading resistance model, allowing accurate extraction of the contact resistivity, which is the sum of the desired metal oxide/$p^+$-Si contact resistivity, the bulk oxide, and the oxide/Al contact.

To analyze the effect of the $p^+$-doping density in the p-type wafer on the contact resistivity with $TiO_2$ (Fig. 4B), p-Si wafers with a uniform doping in the bulk material and Ag were deposited on the $p^+$-Si side to ensure good ohmic contact with low-doping density p-type Si wafers (~$4.0 \times 10^{18}$ and ~$5.3 \times 10^{17}$ $cm^{-3}$).

## Electrochemical capacitance voltage

The capacitance voltage measurement was performed with a Wafer Profiler CVP21, using 0.1 M ammonium bifluoride (ABF or $NH_4$-H-$F_2$) as an electrolyte, allowing for electrical contact to the sample. The 0.1 M solution was made by diluting a 1 M solution in deionized (DI) water by a ratio of 1:9 (1 M ABF:DI water). During the measurement, a voltage was applied, resulting in the ABF contacting the wafer to form localized HF, which was used to etch the sample.

## Si lifetime measurements

The minority-carrier lifetime ($\tau_{eff}$) and the implied $V_{oc}$ of the passivated and unpassivated samples were measured as a function of the minority carrier injection level ($\Delta n$) on a Sinton Instruments WCT120 photoconductance apparatus operating in transient mode. The substrate was n-type Si with boron doping on both sides using the same doping process described above for the tandem device fabrication. The samples

were tested with or without the ALD-$TiO_2$ capping layer deposited symmetrically on both sides.

### Hall effect measurement

For Hall effect measurements, ALD-$TiO_2$ films with a thickness of ~100 nm were deposited on clean quartz slides. The quartz substrates were cleaned sequentially with detergent, acetone, isopropyl alcohol, and ethanol in an ultrasonic bath, with each process lasting for 15 min. The substrates were then treated with ultraviolet (UV) ozone for 30 min to minimize any residual contamination. The annealed samples were then heated at 400°C for 20 min to replicate the tandem solar cell fabrication conditions. Ag was used as the contact with the $TiO_2$ film. Measurements were conducted immediately after the samples were fabricated to minimize exposure to air.

Hall effect and resistivity measurements were then performed using a four-contact van der Pauw configuration with a Lake Shore 7704A analyzer. Throughout the measurement, the magnetic field was kept between 0.1 and 0.5 T, positive to negative, to remove the influence of a misalignment voltage. Samples were measured at room temperature in air in the dark.

### Atomic force microscopy

The morphology mapping of the ALD-$TiO_2$ film and the perovskite on different substrates (Si or FTO substrate) was performed in air using a Cypher AFM (atomic force microscopy) system (Asylum Research). Olympus AC240TM conductive silicon probes (tip coating, 5 nm/20 nm Ti/Pt; force constant, calibrated 1.8 N $m^{-1}$) were used.

### Electron microscopy

Cross sections of the $TiO_2$/$p^+$-Si interface were prepared using the focused ion beam (FIB) lift-out technique in a Helios NanoLab 600 Dual Beam SEM/FIB system. Final thinning of the sample was performed with a $Ga^+$ voltage of 2 kV to minimize surface damage and Ga implantation. STEM examination was carried out using an aberration-corrected JEOL ARM200F microscope operating at 80 kV to minimize radiation damage to the specimens. The instrument was fitted with a cold field-emission electron source. This was coupled to a Noran System Seven analytical system. All imaging and analyses were performed in STEM mode using a high-resolution imaging probe of approximately 30-pA current and 0.1-nm diameter with a convergence semiangle of 24.9 mrad. Imaging was carried out in BF yielding diffraction contrast information. The acceptance semiangle for BF imaging was 17 mrad. Scanning images were captured using Gatan's DigiScan hardware and DigitalMicrograph software.

### X-ray diffraction

X-ray diffraction (XRD) measurements of thin films were obtained using a PANalytical X'Pert Pro system in the grazing incidence angle configuration. Copper Kα x-rays were generated at a tube voltage of 30 kV and a tube current of 10 mA. Scans were performed with 2θ varying from 10° to 80° with a 0.02° step and at a scan speed of 2.3° $min^{-1}$. The $TiO_2$ or ITO films were tested on $p^+$-Si substrates, replicating the conditions during cell fabrication.

### X-ray photoelectron spectroscopy

XPS measurement was obtained in ultrahigh vacuum with a SPECS PHOIBOS-HSA3500 analyzer, recording the electrons with a pass energy of 10 eV. The tested $TiO_2$ films were stored in the vacuum condition before being transferred to the measurement chamber. After being transferred to the chamber, the annealed $TiO_2$ samples were heated under vacuum conditions to 300°C for 20 min to minimize the potential carbon or moisture contamination, while the as-deposited $TiO_2$ films were heated at 150°C for 20 min. The x-ray source was the Mg Kα line with an excitation energy of 1253.6 eV. The XPSs were referenced to the carbon 1s peak at 285.0 eV and the relative concentration of element was normalized with atomic sensitivity factors to account for the variation in cross sections.

### UV light photoelectron spectroscopy

For UPS measurement, a cold cathode with two-stage discharge was used to emit HeI UV photons, and a single photon generates an electron from the corresponding valence level. The electrons were recorded by the PHOIBOS-HSA3500 analyzer with a pass energy of 10 eV. The excitation energy in the UPS experiment was 21.218 eV. The energy cutoff of the valence band signal was used to determine the valence band structure.

### Inverse photoemission spectroscopy

Inverse photoemission spectroscopy was used to determine the unoccupied density of states between the Fermi level and the vacuum level and to characterize the conduction band structure of the sample surface. Acetone was embodied in Ar and was used as the ionizing gas for detection with a photon energy of ~7.9 eV.

### Optical measurement

Reflectance spectra were measured with a PerkinElmer Lambda 1050 spectrophotometer with an integrating sphere detector.

### Photovoltaic performance measurement

The current-voltage characteristics of the cells were measured using a solar simulator system (model no. SS150, Photo Emission Tech Inc.) equipped with a potentiostat source (Autolab PGSTAT302N). The light intensity was calibrated at 1 sun (AM1.5G, 100 mW $cm^{-2}$) using a certified Fraunhofer CalLab reference cell. Both single-junction and perovskite/Si tandem were measured using a custom-built measurement apparatus, with controllable temperature. The atmosphere could be switched from air to $N_2$. The scanning speed and direction were controlled by Autolab potentiostat. All the devices were measured without any preconditioning, after reaching equilibrium at open-circuit conditions.

### EQE measurements

External quantum efficiency (EQE) spectra of the perovskite solar cells were obtained using a homemade setup without light bias in a DC mode using a tungsten light source, a SP AB301-T monochromator, two Keithey 2425 source meters, and a Si reference cell. The system was calibrated using a certified Fraunhofer CalLab reference cell. The EQE spectra of the silicon subcell were measured in a temperature-controlled and nitrogen-filled apparatus with a Protoflex QE1400 system in conjunction with a lock-in amplifier in AC mode (270 Hz). We first illuminated the tandem device with a blue light-emitting diode chip (peak emission at 450 nm) housed with a shortpass filter (Thorlabs FES0500) to provide sufficient current for the perovskite subcell. The battery power supply and a current meter were then connected in series with the cell and the lock-in amplifier to address artifacts that might occur because of relatively small shunt resistance in the tandem device. A forward bias voltage was then applied and adjusted until negligible current (10 nA) was recorded. After the setup had been completed, EQE measurements were performed (*13*).

## SUPPLEMENTARY MATERIALS

Supplementary material for this article is available at http://advances.sciencemag.org/cgi/content/full/4/12/eaau9711/DC1

Fig. S1. Morphologies of $TiO_2$, cross-sectional $TiO_2$/Si interface, and perovskite solar cell.
Fig. S2. XRD patterns of $TiO_2$ and ITO films and perovskite morphology on different substrates.
Fig. S3. Photovoltaic performance of single-junction perovskite solar cells.
Fig. S4. Structure and photovoltaic performance of Si homojunction device and corresponding tandem device.
Fig. S5. Passivation and contact behaviors with optimized $TiO_2$ film and poly-Si substrate.
Fig. S6. Damp heat test of an encapsulated semitransparent perovskite solar cell.
Fig. S7. Histogram of stability test for four perovskite solar cells.
Fig. S8. Light-soaking: Irradiance test of perovskite solar cell.
Fig. S9. Stability test of nonencapsulated perovskite/Si tandem solar cell.
Fig. S10. Contact behavior of p-Si and various $TiO_2$ films and *J-V* curves of corresponding tandem devices.
Fig. S11. XPS analysis of different $TiO_2$ films fabricated with different ALD precursors.
Fig. S12. Energy level analysis of $TiO_2$ films fabricated with different precursors.
Fig. S13. Contact behavior and energetics analysis of $TiCl_4$-ALD $TiO_2$ films deposited at different temperatures.
Fig. S14. Effect of ms-$TiO_2$ on the performance of different tandem devices.
Fig. S15. Simulation of the effect of tunneling on the contact behavior.
Table S1. Hysteresis behavior of a tandem device.
Table S2. Electrical properties of as-deposited $TiO_2$.
Table S3. Electrical properties of annealed $TiO_2$.
References (*41*–*46*)

## REFERENCES AND NOTES


1. K. Yoshikawa, H. Kawasaki, W. Yoshida, T. Irie, K. Konishi, K. Nakano, T. Uto, D. Adachi, M. Kanematsu, H. Uzu, K. Yamamoto, Silicon heterojunction solar cell with interdigitated back contacts for a photoconversion efficiency over 26%. *Nat. Energy* **2**, 17032 (2017).
2. S. Essig, C. Allebé, T. Remo, J. F. Geisz, M. A. Steiner, K. Horowitz, L. Barraud, J. S. Ward, M. Schnabel, A. Descoeudres, D. L. Young, M. Woodhouse, M. Despeisse, C. Ballif, A. Tamboli, Raising the one-sun conversion efficiency of III–V/Si solar cells to 32.8% for two junctions and 35.9% for three junctions. *Nat. Energy* **2**, 17144 (2017).
3. A. Kojima, K. Teshima, Y. Shirai, T. Miyasaka, Organometal halide perovskites as visible-light sensitizers for photovoltaic cells. *J. Am. Chem. Soc.* **131**, 6050–6051 (2009).
4. H.-S. Kim, C.-R. Lee, J.-H. Im, K.-B. Lee, T. Moehl, A. Marchioro, S.-J. Moon, R. Humphry-Baker, J.-H. Yum, J. E. Moser, M. Grätzel, N.-G. Park, Lead iodide perovskite sensitized all-solid-state submicron thin film mesoscopic solar cell with efficiency exceeding 9%. *Sci. Rep.* **2**, 591 (2012).
5. M. M. Lee, J. Teuscher, T. Miyasaka, T. N. Murakami, H. J. Snaith, Efficient hybrid solar cells based on meso-superstructured organometal halide perovskites. *Science* **338**, 643–647 (2012).
6. Oxford PV, "Oxford PV sets world record for perovskite solar cell," 25 June 2018; www.oxfordpv.com/news/oxford-pv-sets-world-record-perovskite-solar-cell.
7. M. Saliba, T. Matsui, K. Domanski, J.-Y. Seo, A. Ummadisingu, S. M. Zakeeruddin, J.-P. Correa-Baena, W. R. Tress, A. Abate, A. Hagfeldt, M. Grätzel, Incorporation of rubidium cations into perovskite solar cells improves photovoltaic performance. *Science* **354**, 206–209 (2016).
8. K. A. Bush, A. F. Palmstrom, Z. Yu, M. Boccard, R. Cheacharoen, J. P. Mailoa, D. P. McMeekin, R. L. Z. Hoye, C. D. Bailie, T. Leijtens, I. M. Peters, M. C. Minichetti, N. Rolston, R. Prasanna, S. Sofia, D. Harwood, W. Ma, F. Moghadam, H. J. Snaith, T. Buonassisi, Z. Holman, S. F. Bent, M. D. McGehee, 23.6%-efficient monolithic perovskite/silicon tandem solar cells with improved stability. *Nat. Energy* **2**, 17009 (2017).
9. National Renewable Energy Laboratory, "Best Research-Cell Efficiencies" (2018); www.nrel.gov/pv/assets/pdfs/pv-efficiencies-07-17-2018.pdf.
10. J. P. Mailoa, C. D. Bailie, E. C. Johlin, E. T. Hoke, A. J. Akey, W. H. Nguyen, M. D. McGehee, T. Buonassisi, A 2-terminal perovskite/silicon multijunction solar cell enabled by a silicon tunnel junction. *Appl. Phys. Lett.* **106**, 121105 (2015).
11. F. Sahli, B. A. Kamino, J. Werner, M. Bräuninger, B. Paviet-Salomon, L. Barraud, R. Monnard, J. P. Seif, A. Tomasi, Q. Jeangros, A. Hessler-Wyser, S. De Wolf, M. Despeisse, S. Nicolay, B. Niesen, C. Ballif, Improved optics in monolithic perovskite/silicon tandem solar cells with a nanocrystalline silicon recombination junction. *Adv. Energy Mater.* **8**, 1701609 (2018).
12. F. Sahli, J. Werner, B. A. Kamino, M. Bräuninger, R. Monnard, B. Paviet-Salomon, L. Barraud, L. Ding, J. J. Diaz Leon, D. Sacchetto, G. Cattaneo, M. Despeisse, M. Boccard, S. Nicolay, Q. Jeangros, B. Niesen, C. Ballif, Fully textured monolithic perovskite/silicon tandem solar cells with 25.2% power conversion efficiency. *Nat. Mater.* **17**, 820–826 (2018).
13. Y. Wu, D. Yan, J. Peng, T. Duong, Y. Wan, S. P. Phang, H. Shen, N. Wu, C. Barugkin, X. Fu, S. Surve, D. Grant, D. Walter, T. P. White, K. R. Catchpole, K. J. Weber, Monolithic perovskite/silicon-homojunction tandem solar cell with over 22% efficiency. *Energy Environ. Sci.* **10**, 2472–2479 (2017).
14. S. Albrecht, M. Saliba, J. P. Correa Baena, F. Lang, L. Kegelmann, M. Mews, L. Steier, A. Abate, J. Rappich, L. Korte, R. Schlatmann, M. K. Nazeeruddin, A. Hagfeldt, M. Grätzel, B. Rech, Monolithic perovskite/silicon-heterojunction tandem solar cells processed at low temperature. *Energy Environ. Sci.* **9**, 81–88 (2016).
15. J. Werner, C.-H. Weng, A. Walter, L. Fesquet, J. P. Seif, S. De Wolf, B. Niesen, C. Ballif, Efficient monolithic perovskite/silicon tandem solar cell with cell area >1 $cm^2$. *J. Phys. Chem. Lett.* **7**, 161–166 (2016).
16. S. Hu, M. R. Shaner, J. A. Beardslee, M. Lichterman, B. S. Brunschwig, N. S. Lewis, Amorphous $TiO_2$ coatings stabilize Si, GaAs, and GaP photoanodes for efficient water oxidation. *Science* **344**, 1005–1009 (2014).
17. M. T. McDowell, M. F. Lichterman, A. I. Carim, R. Liu, S. Hu, B. S. Brunschwig, N. S. Lewis, The influence of structure and processing on the behavior of $TiO_2$ protective layers for stabilization of n-Si/$TiO_2$/Ni photoanodes for water oxidation. *ACS Appl. Mater. Interfaces* **7**, 15189–15199 (2015).
18. D. Yan, A. Cuevas, Y. Wan, J. Bullock, Passivating contacts for silicon solar cells based on boron-diffused recrystallized amorphous silicon and thin dielectric interlayers. *Sol. Energy Mater. Sol. Cells* **152**, 73–79 (2016).
19. J. Peng, Y. Wu, W. Ye, D. A. Jacobs, H. Shen, X. Fu, Y. Wan, T. Duong, N. Wu, C. Barugkin, H. T. Nguyen, D. Zhong, J. Li, T. Lu, Y. Liu, M. N. Lockrey, K. J. Weber, K. R. Catchpole, T. P. White, Interface passivation using ultrathin polymer–fullerene films for high-efficiency perovskite solar cells with negligible hysteresis. *Energy Environ. Sci.* **10**, 1792–1800 (2017).
20. H. Shen, T. Duong, J. Peng, D. Jacobs, N. Wu, J. Gong, Y. Wu, S. K. Karuturi, X. Fu, K. Weber, X. Xiao, T. P. White, K. Catchpole, Mechanically-stacked perovskite/CIGS tandem solar cells with efficiency of 23.9% and reduced oxygen sensitivity. *Energy Environ. Sci.* **11**, 394–406 (2018).
21. J. Werner, B. Niesen, C. Ballif, Perovskite/silicon tandem solar cells: Marriage of convenience or true love story? – An overview. *Adv. Mater. Interfaces* **5**, 1700731 (2018).
22. T. Duong, Y. Wu, H. Shen, J. Peng, X. Fu, D. Jacobs, E.-C. Wang, T. C. Kho, K. C. Fong, M. Stocks, E. Franklin, A. Blakers, N. Zin, K. McIntosh, W. Li, Y.-B. Cheng, T. P. White, K. Weber, K. Catchpole, Rubidium multication perovskite with optimized bandgap for perovskite-silicon tandem with over 26% efficiency. *Adv. Energy Mater.* **7**, 1700228 (2017).
23. Y. Zhou, Y.-H. Jia, H.-H. Fang, M. A. Loi, F.-Y. Xie, L. Gong, M.-C. Qin, X.-H. Lu, C.-P. Wong, N. Zhao, Composition-tuned wide bandgap perovskites: From grain engineering to stability and performance improvement. *Adv. Funct. Mater.* **28**, 1803130 (2018).
24. J. Melskens, B. W. H. van de Loo, B. Macco, L. E. Black, S. Smit, W. M. M. Kessels, Passivating contacts for crystalline silicon solar cells: From concepts and materials to prospects. *IEEE J. Photovolt.* **8**, 373–388 (2018).
25. J. A. Christians, P. Schulz, J. S. Tinkham, T. H. Schloemer, S. P. Harvey, B. J. Tremolet de Villers, A. Sellinger, J. J. Berry, J. M. Luther, Tailored interfaces of unencapsulated perovskite solar cells for >1,000 hour operational stability. *Nat. Energy* **3**, 68–74 (2018).
26. S. Mokkapati, K. R. Catchpole, Nanophotonic light trapping in solar cells. *J. Appl. Phys.* **112**, 101101 (2012).
27. D. T. Grant, K. R. Catchpole, K. J. Weber, T. P. White, Design guidelines for perovskite/silicon 2-terminal tandem solar cells: An optical study. *Opt. Express* **24**, A1454–A1470 (2016).
28. J. Jhaveri, S. Avasthi, G. Man, W. E. McClain, K. Nagamatsu, A. Kahn, J. Schwartz, J. C. Sturm, Hole-blocking crystalline-silicon/titanium-oxide heterojunction with very low interface recombination velocity, in *IEEE 39th Photovoltaic Specialists Conference (PVSC)* (IEEE, 2013), pp. 3292–3296.
29. J. A. Willemen, M. Zeman, J. W. Metselaar, *Proceedings of 1994 IEEE 1st World Conference on Photovoltaic Energy Conversion - WCPEC (A Joint Conference of PVSC, PVSEC and PSEC)* (IEEE, 1994).
30. R. H. Cox, H. Strack, Ohmic contacts for GaAs devices. *Solid-State Electron.* **10**, 1213–1218 (1967).
31. M. Perego, G. Seguini, G. Scarel, M. Fanciulli, F. Wallrapp, Energy band alignment at $TiO_2$/Si interface with various interlayers. *J. Appl. Phys.* **103**, 043509 (2008).
32. B. Mei, T. Pedersen, P. Malacrida, D. Bae, R. Frydendal, O. Hansen, P. C. K. Vesborg, B. Seger, I. Chorkendorff, Crystalline $TiO_2$: A generic and effective electron-conducting protection layer for photoanodes and -cathodes. *J. Phys. Chem. Rev.* **119**, 15019–15027 (2015).
33. J. M. O. Zide, A. Kleiman-Shwarsctein, N. C. Strandwitz, J. D. Zimmerman, T. Steenblock-Smith, A. C. Gossard, A. Forman, A. Ivanovskaya, G. D. Stucky, Increased efficiency in multijunction solar cells through the incorporation of semimetallic ErAs nanoparticles into the tunnel junction. *Appl. Phys. Lett.* **88**, 162103 (2006).
34. R. T. Tung, The physics and chemistry of the Schottky barrier height. *Appl. Phys. Rev.* **1**, 011304 (2014).
35. L.-Å. Ragnarsson, P. Lundgren, Electrical characterization of $P_b$ centers in (100)Si-$SiO_2$ structures: The influence of surface potential on passivation during post metallization anneal. *J. Appl. Phys.* **88**, 938–942 (2000).
36. P. Kohn, S. Pathak, M. Stefik, C. Ducati, U. Wiesner, U. Steiner,S. Guldin, Low temperature crystallisation of mesoporous $TiO_2$. *Nanoscale* **5**, 10518–10524 (2013).

37. D. Pérez-del-Rey, P. P. Boix, M. Sessolo, A. Hadipour,H. J. Bolink, Interfacial modification for high-efficiency vapor-phase-deposited perovskite solar cells based on a metal oxide buffer layer. *J. Phys. Chem. Lett.* **9**, 1041–1046 (2018).
38. S. You, H. Wang, S. Bi, J. Zhou, L. Qin, X. Qiu, Z. Zhao, Y. Xu, Y. Zhang, X. Shi, H. Zhou, Z. Tang, A biopolymer heparin sodium interlayer anchoring $TiO_2$ and $MAPbI_3$ enhances trap passivation and device stability in perovskite solar cells. *Adv. Mater.* **30**, 1706924 (2018).
39. M. A. Green, Accuracy of analytical expressions for solar cell fill factors. *Sol. Cells* **7**, 337–340 (1982).
40. J. Zheng, C. F. J. Lau, H. Mehrvarz, F.-J. Ma, Y. Jiang, X. Deng, A. Soeriyadi, J. Kim, M. Zhang, L. Hu, X. Cui, D. S. Lee, J. Bing, Y. Cho, C. Chen, M. A. Green, S. Huang, A. W. Y. Ho-Baillie, Large area efficient interface layer free monolithic perovskite/homo-junction-silicon tandem solar cell with over 20% efficiency. *Energy Environ. Sci.* **11**, 2432–2443 (2018).
41. W. Ahmad, J. Khan, G. Niu, J. Tang, Inorganic $CsPbI_3$ perovskite-based solar cells: A choice for a tandem device. *Sol. RRL* **1**, 1700048 (2017).
42. W. S. Yang, B.-W. Park, E. H. Jung, N. J. Jeon, Y. C. Kim, D. U. Lee, S. S. Shin, J. Seo, E. K. Kim, J. H. Noh, S. I. Seok, Iodide management in formamidinium-lead-halide–based perovskite layers for efficient solar cells. *Science* **356**, 1376–1379 (2017).
43. X. Zhao, H.-S. Kim, J.-Y. Seo, N.-G. Park, Effect of selective contacts on the thermal stability of perovskite solar cells. *ACS Appl. Mater. Interfaces* **9**, 7148–7153 (2017).
44. M. Jung, T. J. Shin, J. Seo, G. Kim, S. I. Seok, Structural features and their functions in surfactant-armoured methylammonium lead iodide perovskites for highly efficient and stable solar cells. *Energy Environ. Sci.* **11**, 2188–2197 (2018).
45. K. Domanski, E. A. Alharbi, A. Hagfeldt, M. Grätzel, W. Tress, Systematic investigation of the impact of operation conditions on the degradation behaviour of perovskite solar cells. *Nat. Energy* **3**, 61–67 (2018).
46. T. Leijtens, G. E. Eperon, S. Pathak, A. Abate, M. M. Lee, H. J. Snaith, Overcoming ultraviolet light instability of sensitized $TiO_2$ with meso-superstructured organometal tri-halide perovskite solar cells. *Nat. Commun.* **4**, 2885 (2013).


**Acknowledgments:** We would like to thank S. Surve for the mask fabrication and D. Sheng for the STEM results discussion. We greatly appreciate T. Lu and Y. Liu for help with the AFM measurement, D. Walter and T. Kho for discussion about the passivation of Si solar cells, P. Zhang, Y. Zhang, and L. Wang for coordination of the EQE measurement, W. Liang for optimization of the texturing process, and H. T. Nguyen for optical analysis. The electron spectroscopy apparatus was built with a grant from the Australian Research Council (LE0989068). We acknowledge the equipment and support provided by the Australian Microscopy and Microanalysis Research Facility (AMMRF) and the Australian National Fabrication Facility (ANFF) at the South Australian nodes of the AMMRF and ANFF under the National Collaborative Research Infrastructure Strategy. **Funding:** This work was supported by the Australian Government through the Australian Renewable Energy Agency (ARENA), grant MG005, and the Australian Research Council through grant FT13010916. Responsibility for the views, information, or advice expressed herein is not accepted by the Australian Government. Part of the experiment was performed at ANFF ACT Node at the Australian National University. The conception and experimental realization of the $TiO_2$ deposition and ohmic contact behavior in the tandem solid-state device structure are based on work performed by the Joint Center for Artificial Photosynthesis, a DOE Energy Innovation Hub, supported through the Office of Science of the U.S. Department of Energy under award no. DE-SC0004993. **Author contributions:** N.S.L. and K.R.C. supervised the research and coordinated the collaboration. N.S.L., S.T.O., and S.Y. were instrumental in generating the concept for this work. H.S. designed experiments as well as fabricated and characterized devices. D.A.J. helped with data analysis, provided the physical theory, and performed simulations. S.T.O., S.Y., N.W., and Y.Wa. contributed to preparing different $TiO_2$ materials and the design of experiments to characterize the $TiO_2$/Si contacts. Y.Wa., Y.Wu, T.D., and T.P.W. supplied expertise in tandem design. P.P., C.S., Y.Wu, and D.Y. helped with Si solar cell design and fabrication. T.D. and J.P. assisted in perovskite device fabrication and device stability analysis. Y.Y. and G.G.A. were responsible for the energy level characterization of the ALD-$TiO_2$ layer. H.S. and D.A.J. prepared the manuscript, and N.S.L, K.R.C., S.T.O., and S.Y. helped with its editing. All authors reviewed and contributed to the final manuscript. **Competing interests:** S.T.O., S.Y., and N.S.L. are inventors on a provisional U.S. patent application related to this work filed by the California Institute of Technology (no. 62/662,852, filed 26 April 2018). The authors declare that there are no other competing interests. **Data and materials availability:** All data needed to evaluate the conclusions in the paper are present in the paper and/or the Supplementary Materials. Additional data related to this paper may be requested from the authors.

Submitted 1 August 2018
Accepted 15 November 2018
Published 14 December 2018
10.1126/sciadv.aau9711

**Citation:** H. Shen, S. T. Omelchenko, D. A. Jacobs, S. Yalamanchili, Y. Wan, D. Yan, P. Phang, T. Duong, Y. Wu, Y. Yin, C. Samundsett, J. Peng, N. Wu, T. P. White, G. G. Andersson, N. S. Lewis, K. R. Catchpole, In situ recombination junction between p-Si and $TiO_2$ enables high-efficiency monolithic perovskite/Si tandem cells. *Sci. Adv.* **4**, eaau9711 (2018).

Science Advances

# In situ recombination junction between p-Si and $TiO_2$ enables high-efficiency monolithic perovskite/Si tandem cells

Heping Shen, Stefan T. Omelchenko, Daniel A. Jacobs, Sisir Yalamanchili, Yimao Wan, Di Yan, Pheng Phang, The Duong, Yiliang Wu, Yanting Yin, Christian Samundsett, Jun Peng, Nandi Wu, Thomas P. White, Gunther G. Andersson, Nathan S. Lewis and Kylie R. Catchpole

*Sci Adv* **4** (12), eaau9711.
DOI: 10.1126/sciadv.aau9711